Design and Data Processing of China's First Spaceborne Laser Altimeter System for Earth Observation: GaoFen-7

Junfeng Xie, Genghua Huang, Ren Liu, Chenguang Zhao, Jun Dai, Taoyong Jin, Fan Mo, Ying Zhen, Shaoli Xi, Hongzhao Tang, Xianhui Dou, and Chenchen Yang

***Abstract*—The GaoFen-7 (GF-7) satellite, which was launched on November 3, 2019, is China's first civilian submeter stereo mapping satellite. The satellite is equipped with the first laser altimeter officially in China for earth observation. Except for the laser altimeter, the GF-7 spaceborne laser altimeter system also includes two laser footprint cameras and a laser optical axis surveillance camera. The laser altimeter system is designed and used to assist improving the elevation accuracy without ground control points of the two line-array stereo mapping cameras. This article details the design of the GF-7 spaceborne laser altimeter system, its ranging performance in the laboratory, and its data processing method. The type of data products is also released. These data will play a vital role in the application of geography, glaciology, forestry, and other industries.**

***Index Terms*—Data processing, footprint camera, GF-7 satellite, laser altimeter, laser products, optical axis surveillance camera.**

I. Introduction

THE GF-7 satellite is the first submeter-level resolution mapping satellite in the Medium- and Long-Term Development Plan for China's Civil Space Infrastructure (2015–2025) [1]. The satellite is equipped with two main payload systems. The one is the two line-array stereo mapping cameras and the other is a laser altimeter system. The two line-array camera will provide stereoscopic panchromatic images at a resolution of 0.7 m, whereas the laser altimeter system will provide high-accuracy ranging data, digitized echo waveforms with 2 GHz sampling rate, and laser footprints images at a resolution of 3.2 m. The combination of the laser altimeter and stereo camera will be mainly used for 1:10 000 stereo mapping of China and large-scale geographic information data updating.

In China, the GF-7 spaceborne laser altimeter system will be officially and first used for Earth observations, whereas the Ziyuan3-02 (ZY3-02) spaceborne laser altimeter is considered as the test payload. The main payload of the ZY3-02 satellite is a three-line array mapping camera for capturing high-resolution stereo images [2]–[4]. The GF-7 spaceborne laser altimeter system main mission is to perform topographic surveying and assist optical image to improving the mapping elevation accuracy without GCPs. Moreover, it will be used to monitor polar ice sheet change [5], forest biomass inversion [6], and ocean lakes [7]. The diagram of the GF-7 laser altimeter system is shown in Fig. 1. The GF-7 spaceborne laser altimeter system employs dual beams, and the angle between each beam and the nadir is 0.7°. The transmitted laser pulse illuminates a spot on the Earth's surface, with a diameter of 17.5 m (@500 km), except when optically thick clouds obscure the surface. When the energy of return pulse is strong enough, a linear detection mode based on an avalanche photodiode (APD) loaded on GF-7 satellite has been applied in converting the return pulse to an analog waveform [8]. Successive spots are separated on the Earth's surface by 2.4 km, and the beam pairs are further separated by approximately 12.25 km in the cross-track direction. Moreover, the laser footprint camera (LFC) photographs the laser footprint and surface features at the moment of laser transmittal, and it can be used to connect and construct the geometric relationship between the laser footprints and the line-array stereo mapping camera. Similarly, the laser optical axis surveillance camera (LOASC) also acquires an image of two laser beam without surface features to analyze laser pointing stability. The basic parameter and performance of the GF-7 spaceborne laser altimeter system will be introduced. According to three types of payload in the GF-7 spaceborne laser altimeter system, this article details the processing flow and methods of the different data when

Manuscript received September 18, 2019; revised December 23, 2019 and February 16, 2020; accepted February 24, 2020. Date of publication March 9, 2020; date of current version March 21, 2020. This work was supported in part by the National Natural Science Foundation of China under Grant 41971426, in part by the Authenticity Validation Technology of Elevation Accuracy of the GF-7 Laser Altimeter under Grant 42-Y20A11-9001-17/18, in part by the active and passive composite mapping and application technology with visible, infrared and laser sensors under Grant D040106, in part by the Class B Project of Beijing Science and Technology Association Jinqiao Project Seed Fund under Grant ZZ19013, and in part by the multibeam terrain detection laser and its application technology under Grant D040105. *(Corresponding author: Ren Liu.)*

Junfeng Xie is with the Land Satellite Remote Sensing Application Center, Ministry of Natural Resources of P. R. China, Beijing 100048, China, and also with the School of Geomatics, Liaoning Technical University, Fuxin 123000, China (e-mail: junfeng_xie@163.com).

Genghua Huang is with the Shanghai Institute of Technical Physics, Chinese Academy of Science, Shanghai 200083, China (e-mail: genghuah@mail.sitp.ac.cn).

Ren Liu is with the School of Earth Sciences and Engineering, Hohai University, Nanjing 211100, China (e-mail: rs_liur@163.com).

Chenguang Zhao and Jun Dai are with the China Academy of Space Technology, Beijing 100094, China (e-mail: zcg_hit@163.com; haojundj@163.com).

Taoyong Jin is with the School of Geodesy and Geomatics, Wuhan University, Wuhan 430079, China (e-mail: tyjin@sgg.whu.edu.cn).

Fan Mo, Ying Zhen, Shaoli Xi, Hongzhao Tang, Xianhui Dou, and Chenchen Yang are with Land Satellite Remote Sensing Application Center, Ministry of Natural Resources of P. R. China, Beijing 100048, China (e-mail: surveymofan@163.com; z_ying0513@163.com; 892575043@qq.com; 470891156@qq.com; 449269165@qq.com; 571200645@qq.com).

Digital Object Identifier 10.1109/JSTARS.2020.2977935

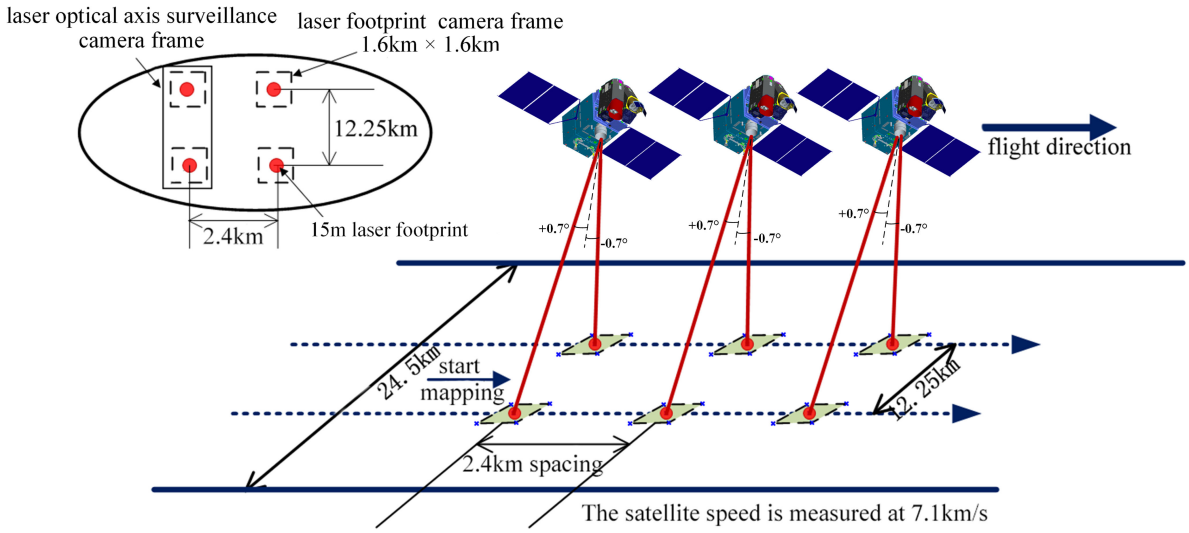

Fig. 1. Schematic diagram of the GF-7 spaceborne laser altimeter system.

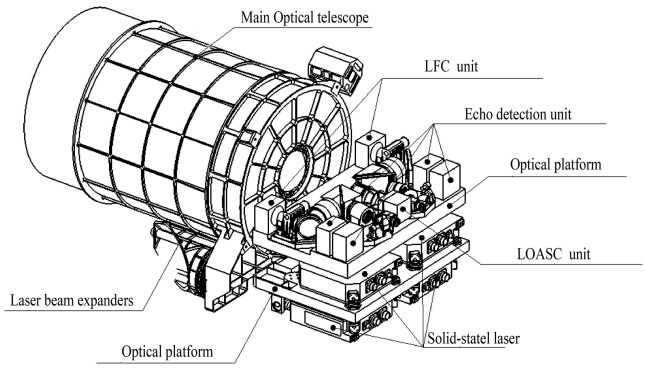

Fig. 2. Main diagram of the GF-7 laser altimeter system.

TABLE I
BASIC DESIGN PARAMETERS OF THE GF-7 LASER ALTIMETER

Parameter	Value
Number of beams	2
Laser Wavelength	1064 nm
Laser energy	100~180 mJ (adjustable)
Emission pulse width	4~8 ns
Laser divergence angle	30~40 μrad
Receiving telescope aperture	600 mm
Pulse repetition frequency	3/6 Hz
Echo digitization interval	0.5 ns
Laser emission efficiency	0.994
Laser receiving efficiency	0.790
Laser ranging range	450~550 km
Laser ranging accuracy	≤0.3 m (Slope less than 15°)

the satellite operates in-orbit. Six-level products are produced based on metadata of the laser system. All of these products will be released globally and widely applied in geography, forestry glaciology, and other industries for the Earth's natural resources monitoring effectively. Ultimately, these products will provide reliable services for the sustainable development of the Earth and human beings.

II. LASER ALTIMETER SYSTEM

The GF-7 spaceborne laser altimeter system consists mainly of two master and two slave lasers and laser receivers, two LFCs, and one LOASC. The LFC and LOASC are used to assist the laser altimeter in locating the laser footprints on the Earth's surface. An optical prism with 0.1% reflection is designed to illuminate the LFC and the LOASC when the laser pulse is emitted. The diagram of the GF-7 spaceborne laser altimeter system is shown in Fig. 2.

A. Overview of the Laser Altimeter Design

The basic design parameters of the GF-7 laser altimeter are given in Table I.

Two active lasers are considered as the master lasers, and they are named master laser 1 (ML-1) and master laser 2 (ML-2) and can operate simultaneously. The other two backups are slave lasers, and they are named slave laser 1 (SL-1) and slave laser 2 (SL-2) and can be switched into the main laser emission path by the switching mechanism. The four lasers are independently controlled by the satellite controller unit. The GF-7 spaceborne laser altimeter system has two beams that are named beam 1 (right-hand side along trace in Fig. 1) and beam 2 (left-hand side along trace in Fig. 1). Beam 1 consists of ML-1 and SL-1, and beam 2 consists of ML-2 and SL-2.

The performances of the laser divergence, beam stability, and ranging accuracy directly determine the positioning accuracy of the spaceborne laser altimeters. The scientific research team (SRT) of the GF-7 spaceborne laser altimeter system had tested many functions and performance indicators of the laser altimeter system in the laboratory.

1) Laser Divergence Angle: For a Gaussian pulse of laser, $1/e^2$ of the peak energy is defined as the boundary of the divergence angle, and about 86% of the laser emission energy is concentrated within the divergence angle. The test results of the GF-7 laser divergence angle in the laboratory are shown in Table II.

TABLE II
MEASUREMENT RESULTS OF THE GF-7 LASER DIVERGENCE ANGLE

Laser	Energy (mJ)	Divergence angle (urad)		
		Horizontal	Vertical	Synthetic
ML-1	180	30	33	33
SL-1	180	42	30	32
ML-2	180	28	23	27
SL-2	180	45	25	31

TABLE III
GF-7 LASER BEAM QUALITY RESULTS

Laser	Beam centroid quality (X, Y) μrad	Laser	Beam centroid quality (X, Y) μrad
ML-1	(1.80,1.55)	ML-2	(1.97,1.54)
SL-2	(1.97,1.74)	SL-2	(1.64,1.67)

TABLE IV
GF-7 LASER RANGING STABILITY RESULTS

Laser	Receiver	Energy (mJ)	Ranging variance (m)
ML-1	MR	180	0.026
SL-1	MR	180	0.029
ML-1	SR	180	0.023
SL-1	SR	180	0.027
ML-2	MR	180	0.020
SL-2	MR	180	0.045
ML-2	SR	180	0.019
SL-2	SR	180	0.047

2) Laser Beam Stability: The centroid position of the laser spot was measured in the laboratory by a collimator and a laser beam profiler. The test results are shown in Table III.

The experimental results show that the centroid variance of the GF-7 laser is less than (1.85 μrad, 1.65 μrad).

3) Laser Ranging Accuracy:

a) Ranging stability: The GF-7 master receiver is referred to as MR, and the slave receiver is referred to as SR. A fixed 10-km length optical fiber is used in the cross-test with the master and slave lasers and the master and slave receivers. The ranging variance of beam 1 and beam 2 is shown in Table IV.

An analysis of the above results shows that the ranging stability of the GF-7 laser altimeter is better than 0.048 m under different combinations.

b) Ranging accuracy by temperature: The GF-7 laser altimeter system uses a constant-temperature crystal oscillator as the reference for the time interval measurement. For the maximum distance of 600 km, the temperature drift of the crystal oscillator is the main factor causing the change of ranging precision. High- and low-temperature tests of the GF-7 laser altimeter's constant-temperature crystal oscillator were carried out, and the results showed that the maximum ranging error caused by the crystal oscillator temperature drift is less than 4.2 cm in a temperature range of -85°C to $+85$°C.

c) Ranging accuracy by slope: The slope of the terrain will lead to the extended echo pulse and the low signal-to-noise ratio (SNR). An echo signal generator is used to simulate the stretched echo pulse. An echo waveform with the lowest SNR at 15° sloped terrain is shown in Fig. 3(a), which was used to calculate range error of laser by peak time comparison. 200 times test was repeated to construct a histogram of ranging errors, as shown in Fig. 3(b).

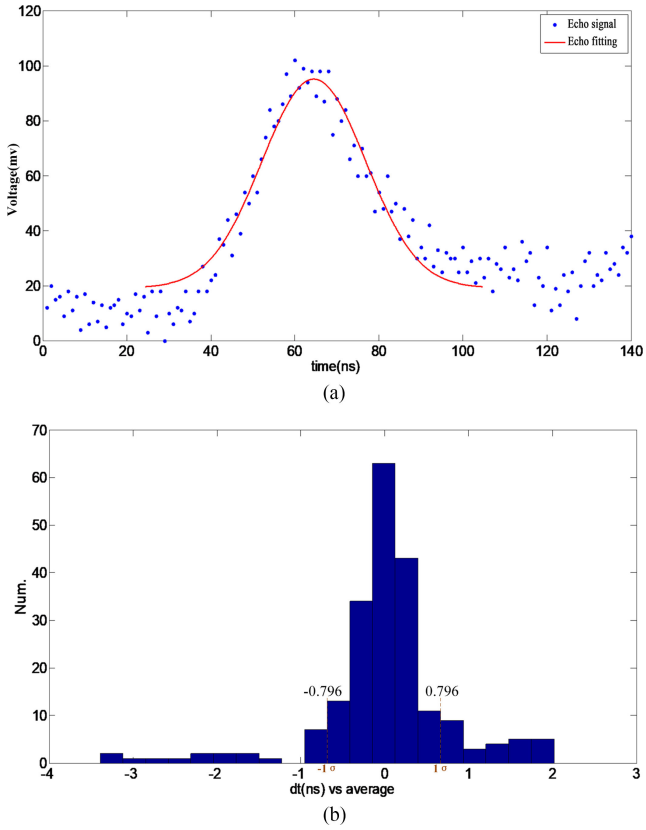

Fig. 3. Ranging accuracy results at the 15° sloped terrain. (a) Echo waveform at the 15° sloped terrain. (b) Distribution of the ranging variance.

According to Fig. 3(b), the test results with the lowest SNR show that the GF-7 spaceborne laser altimeter ranging accuracy achieves to be 0.796 ns (1σ) at the slope of 15° sloped terrain, which is equivalent to a measurement error of 12 cm.

In conclusion, the root-mean-square error (RMSE) of the three kinds of errors above is used to evaluate the ranging accuracy, and the ranging accuracy of the GF-7 spaceborne laser altimeter would be better than 14.0 cm (1σ).

B. Laser Footprint Camera (LFC)

LFC is used to capture the laser spot in synchrony with the laser emission. It constructs the geometric relationship between the laser footprint and the ground object in the image. The basic design parameters are shown in Table V.

The spatial resolution of the LFC is 3.18 m in a 500-km solar synchronous orbit. Two types of imaging modes are designed for different application: 1) an asynchronous exposure imaging mode and 2) a synchronous exposure imaging mode. Mode 1 acquires three images at different times: the remote sensing image before the laser emission (only ground surface information), the laser footprint image synchronizing the laser emission (short exposure time and only laser spot information), and another topographic image after the laser fires (only ground surface information). Mode 2 acquires an image containing the laser footprint and ground surface information at the moment of laser emission.

TABLE V
BASIC DESIGN PARAMETERS OF THE GF-7 LFC AND LOASC

Parameters	LFC	LOASC
Working spectral range	Visible light: 500 - 700 nm & laser: 1064 nm	900 - 1100 nm
Instantaneous field of view	6.4 μrad	6.4 μrad
Modulation Transfer Function (MTF)	≥0.20	N/A
Pixel size	16.5 μm	16.5 μm
Image size	550×550 pixels	550×550 pixels
Field of view (FOV)	±0.1°	±0.1°
Optical aperture	600 mm	600 mm
Number of digits	≥10 bit	≥10 bit
Optical efficiency	≥70%	≥80%
Principal distance	LFC 1: 2580.2 mm LFC 2: 2576.3 mm	N/A

TABLE VI
OPTICAL AXIS MONITORING ACCURACY

Laser	Energy (mJ)	Centroid position mean (pixel)	Centroid position variance (pixel)
ML-1	188	(31.68, 55.39)	(0.13, 0.14)
SL-1	190	(68.50, 39.58)	(0.48, 0.25)
ML-2	186	(58.57, 34.15)	(0.52, 0.50)
SL-2	195	(41.65, 46.82)	(0.4, 0.25)

C. Laser Optical Axis Surveillance Camera (LOASC)

The GF-7 LOASC can also capture footprints from beam 1 and beam 2 passing through the prisms to monitor the stability of the laser emitting the optical axis. The GF-7 LOASC is shown in Fig. 2. The basic parameters of the LOASC are shown in Table V. The LOASC image is a grayscale image that can also be used to observe the laser spot shape.

Table VI shows the results of the centroid positions and the variety of the laser emission axes, measured by the LFC and LOASC in the laboratory. The test was carried out for 15 min at a temperature of 20 °C.

The test results show that the maximum variance is 0.52 pixels, which is equivalent to 0.832 μrad.

III. BASIC DATA PROCESSING AND PRODUCTS

A. General Framework of the GF-7 Laser Altimeter System Data Processing

The GF-7 spaceborne laser altimeter system is equipped with two new LFCs and a LOASC, which present new challenges for GF-7 laser data processing. The general framework of GF-7 laser data processing is shown in Fig. 4. It includes the auxiliary data processing, laser data processing, and image data processing.

B. Laser Data Processing

1) Ranging Data Processing: The spaceborne laser altimeter calculates the ranging between the satellite and earth surface with accurate flight time. According to the geometric relationship between the laser and the satellite platform, combined with precise attitude determination (PAD) and precise orbit determination (POD) data, the 3-D coordinates of the laser footprint can be accurately determined after correcting the error of the atmosphere and tide. However, in-orbit geometry calibration of the spaceborne laser is necessary before the accurate geolocation of the laser spot, which is mainly used to accurately calibrate the pointing and ranging parameters of the laser altimeter.

a) In-orbit geometric laser calibration: The calibration model of the GF-7 laser is constructed with the geometric relationship between the global positioning system (GPS), laser emission reference point, star tracker, satellite platform, laser footprint position, as well as WGS84 ellipsoid. The geometric calibration model of the GF-7 spaceborne laser is shown as [9]

$$\begin{pmatrix} X_{\text{spot}} \\ Y_{\text{spot}} \\ Z_{\text{spot}} \end{pmatrix}_{\text{ITRF}} = \begin{pmatrix} X_s \\ Y_s \\ Z_s \end{pmatrix}_{\text{ITRF}} + R^{\text{ITRF}}_{\text{ICRF}} R^{\text{ICRF}}_{\text{BOD}} \left[\begin{pmatrix} \Delta X_{\text{ref}} \\ \Delta Y_{\text{ref}} \\ \Delta Z_{\text{ref}} \end{pmatrix}_{\text{BOD}} + (\rho_0(t) + \rho_{sy} + \rho_{ot}) \begin{pmatrix} \cos\beta\cos\alpha \\ \cos\beta\sin\alpha \\ \sin\beta \end{pmatrix}_{\text{BOD}} \right] \tag{1}$$

where $(X_{\text{spot}}, Y_{\text{spot}}, Z_{\text{spot}})^T_{\text{ITRF}}$ is the location of the laser footprint in the international terrestrial reference frame (ITRF); $(X_s, Y_s, Z_s)^T_{\text{ITRF}}$ is the position of the satellite centroid in the ITRF; $R^{\text{ICRF}}_{\text{BOD}}$ is the rotation matrix of the satellite body coordinate system in reference to the international celestial reference frame (ICRF); $R^{\text{ITRF}}_{\text{ICRF}}$ is the transition matrix from the ICRF to the ITRF; $(\Delta X_{\text{ref}}, \Delta Y_{\text{ref}}, \Delta Z_{\text{ref}})^T_{\text{BOD}}$ is the offset between the laser emission reference point and the center of the satellite mass in the satellite body coordinate system; $\rho_0(t) \begin{pmatrix} \cos\beta\cos\alpha \\ \cos\beta\sin\alpha \\ \sin\beta \end{pmatrix}_{\text{BOD}}$ is the 3-D coordinates in the satellite body coordinate system, which is centered on the laser emission reference point; $\rho_0(t)$ is the laser range, $\rho_0(t) = c \times \Delta t/2$; c is the speed of light; Δt is the flight time of the laser pulse; ρ_{sy} is the systematic ranging errors that need be calibrated, and they are always caused by time synchronization, hardware measurement error, and other system errors; ρ_{ot} represents the corrections of the atmospheric delay and tidal errors; and α and β are pointing angles of the laser altimeter on the body frame.

The SRT is scheduled to conduct scientific experiments in April 2020, and the laser test program on ice will be implemented in December 2020. On the basis of past experiments, the SRT selected the flat grasslands of the Sonid Youqi in Inner Mongolia and the ice surface of the Khanka Lake in Heilongjiang Province (as shown in Fig. 5) as the calibration test site. Moreover, China's Jiangsu Province was selected as the validation test area, which includes different typical kinds of terrain such as lakes, hills, and mountains. The SRT plans to conduct four types of calibration tests in the above three test areas: 1) Calibration based on terrain matching; 2) Calibration based on an infrared detector; 3) Calibration based on a Corner Cube Retroreflector (CCR); and 4) calibration based on waveform simulation.

The calibration test based on terrain matching will be implemented in the hilly terrain of Jiangsu Province. In 2018, the Land Satellite Remote Sensing Application Center, Ministry of Natural Resources of P. R. China (LASAC), acquired high-precision airborne lidar point cloud data of Jiangsu Province. The SRT

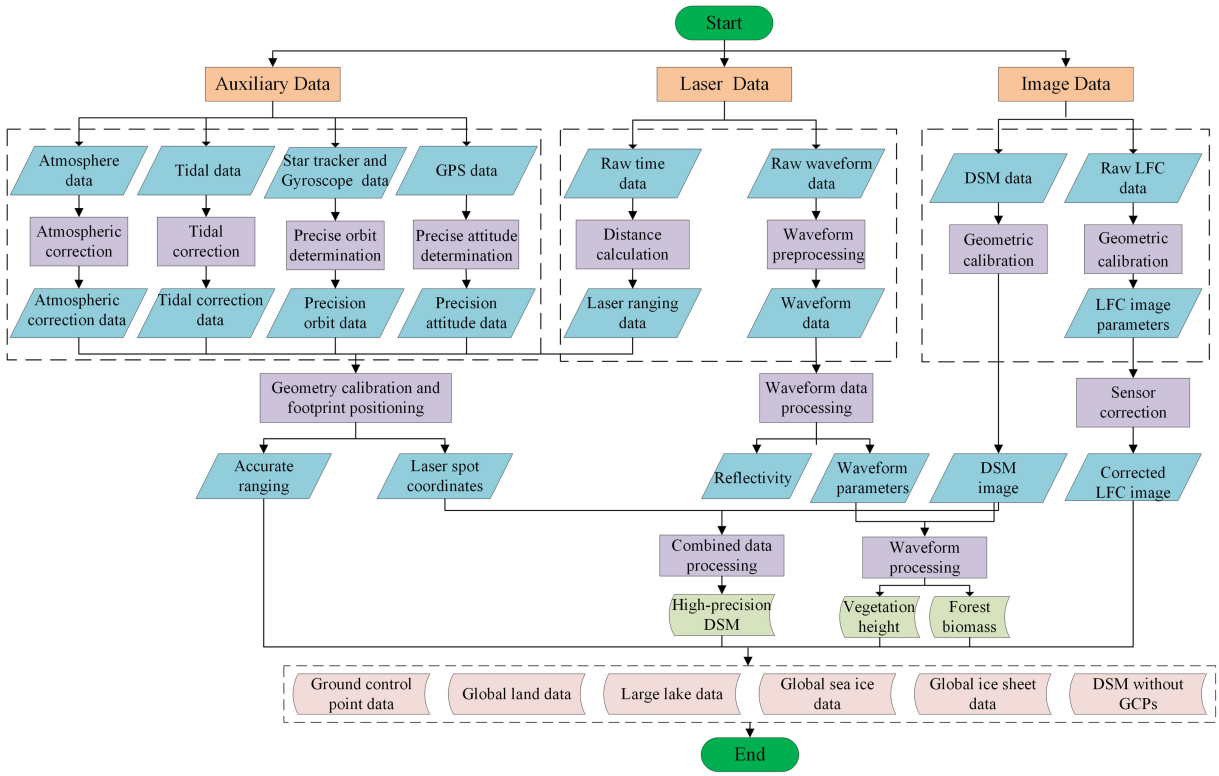

Fig. 4. General framework of the GF-7 laser altimeter system data processing.

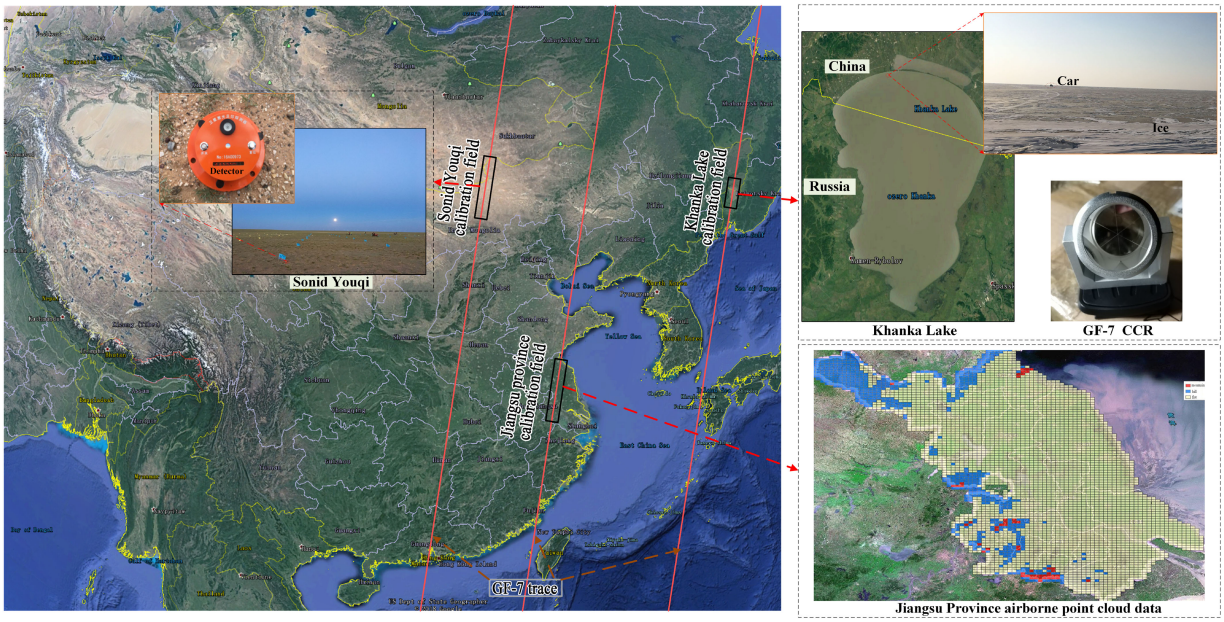

Fig. 5. GF-7 laser calibration test field.

plans to use precisely surveyed terrain matching methods to calibrate the GF-7 laser altimeter pointing and ranging parameters after the satellite is in-orbit [10]. This calibration result will be used for the GF-7 laser ranging data processing.

The test site for the calibration method based on infrared detectors requires flat terrain. Therefore, the open grasslands of Sonid Youqi were selected. The scope of test sites is predicted by predicting the orbit, and attitude data are predicted before the GF-7 satellite flies over the field [11]. Detectors that can capture GF-7 laser signals will be placed in a rectangle array, as shown in Fig. 5. We also plan to place 2600 detectors in a 10 m grid; the grid range is about 800 × 320 m (along-track × across-track). The centroid of laser footprint can be located by the triggered detectors. Then, the calibration parameters are calculated by the

calibration model and the laser footprint centroid location [9], [12]–[14]. Meanwhile, the energy distribution of the GF-7 laser footprint can also be verified.

The LASAC also plans to deploy CCRs on the ice surface of Khanka Lake when the lake froze over in 2020. In addition, 400 CCRs will be placed in a 10 m grid, the grid range is about 320 × 120 m (along-track × across-track). The fields of Khanka Lake in winter and the CCR are shown in the upper right-hand side corner of Fig. 5. According to the echo waveform of the triggered CCR, CCR ground coordinates, satellite orbit and attitude, atmosphere, tide, and other data, the geometric calibration based CCR is completed based on the calibration model [14], [15]. This field test is used to verify and analyze the laser echo energy and calibrate the ranging.

The GF-7 laser altimeter system can record the echo information reflected from the earth surface in the footprint. The SRT plans to carry out waveform simulation to obtain the simulated waveform with DSM of the footprint area, which is compared with the actual recorded echo after the satellite passes over the test field [16], [17]. The laser ranging residual is determined by calculating the waveform offset, and the laser pointing and ranging parameters are calibrated with the calibration model [18]. This method will be mainly used for the verification of the GF-7 laser pointing parameters, which provides a convenient calibration method for GF-7 satellites during in-orbit operation.

b) Laser footprint positioning: By substituting the calibrated pointing and ranging parameters, attitude data, and orbit data at the sampling time of the laser altimeter into (1), the 3-D coordinates of the laser footprint in the WGS 84 coordinate system can be calculated, which are denoted as $[X_{\text{spot}}\ Y_{\text{spot}}\ Z_{\text{spot}}]^T$. It can be converted to the geodetic coordinates $(B\ L\ H)^T$, which is given as [19]

$$\begin{cases} L = \arctan\left(\frac{Y_{\text{spot}}}{X_{\text{spot}}}\right) \\ B = \arctan\left(\frac{Z(N+H)}{\sqrt{(X_{\text{spot}}^2+Y_{\text{spot}}^2)[N(1-e^2)+H]}}\right) \\ H = \frac{\sqrt{X_{\text{spot}}^2+Y_{\text{spot}}^2}}{\cos B} - N \end{cases} \tag{2}$$

where N is the radius of the prime vertical curvature for the WGS-84 ellipsoid, e is the first eccentricity of the WGS-84 ellipsoid, and H is the ellipsoid height of the laser spot. The ground coordinates of GF-7 laser spot can be accurately determined after laser geometric calibration.

2) Waveform Data Processing: The GF-7 spaceborne laser altimeter system records the echo waveform after the laser returns from the ground to the GF-7 satellite. The same laser echo waveform is divided into high- and low-gain waveforms. For the ground surface, there are no more than 1200 bins, and the sampling interval is 0.5 s. The effective one-way distance associated with 1200 bins is 90 m, which represents the maximum elevation change within a single spot that can be recorded. The GF-7 echo waveform can be used to extract the height of the tree and building after waveform decomposition and fitting. High-precision inversion of forest biomass can also be achieved by combining waveforms with high-precision DSM data.

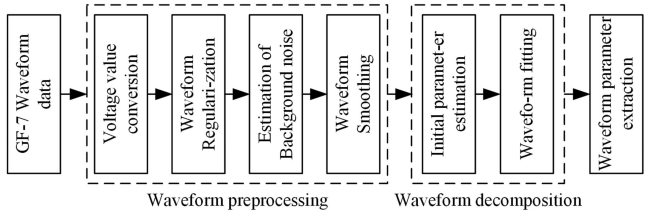

Fig. 6. GF-7 waveform data processing flow.

GF-7 waveform processing mainly includes three parts: waveform preprocessing, waveform decomposition, and waveform parameter extraction. In order to improve the accuracy of waveform decomposition and extracted waveform parameter, waveform preprocessing is first carried out. The waveform parameters after waveform decomposition can be applied to various industries. The overall process of the GF-7 laser waveform processing is shown in Fig. 6.

a) Waveform preprocessing: Voltage conversion refers to the process of converting the amplitude in the waveform from energy intensity to voltage intensity. First, the GF-7 original waveform is sampled and quantified, and its intensity value is converted to a counting range of 0–255 (8 bits).

Waveform regularization is used to eliminate the influence of laser receiving energy difference caused by the environment, instrument, and terrain, which is convenient for the joint application of different shaped echoes. The GF-7 laser echo is regularized to compare with other waveforms under the same standard before application [20].

Noise in the echo waveform is mainly caused by external factors, such as the sensor itself and atmospheric scattering. The statistical histogram method is used to eliminate GF-7 laser echo noise [21]. Waveform is filtered after noise estimation, and the Gaussian filter is used to further remove the noise effects caused by the terrain [22].

b) Waveform decomposition: Over flat terrain, the laser echo waveform is a single Gaussian echo waveform. However, return from terrain that includes hills, mountains, and woodlands, the laser echo waveform is a complex and multipeak waveform. Therefore, echo waveform decomposition is an indispensable process before the application of feature extraction, feature classification, and forest biomass estimation, which is used to estimate the parameters of each decomposed waveform. The SRT plans to adopt several GF-7 waveform decomposition methods, such as Gaussian decomposition, wavelet transform decomposition, and deconvolution [23]–[25]. However, for the echo waveform of complex terrain, the nonlinear least squares method will also be used for waveform-fitting processing [26].

c) Waveform parameter extraction: Waveform parameters play a vital role in the application of tree height estimation and earth carbon storage inversion. The GF-7 spaceborne laser altimeter system is designed for interdisciplinary applications. The SRT plans to extract the basic parameters of the GF-7 laser echo waveform, and these parameters will be available as the level 1A product. These basic parameters mainly include waveform quantile height, waveform height index, and waveform energy index [27]. The waveform quantile height includes

waveform length, wave peak length, and other parameters. The waveform height index mainly includes the full height of the waveform, the height of the half-wave energy, the length of the leading edge of the waveform, the length of the trailing edge of the waveform, and other parameters. The waveform energy index is mainly composed of ground echo energy, relative echo energy, and other parameters.

3) Auxiliary Data Processing: Satellite attitude and orbit error directly affect the final positioning accuracy of the laser footprint. Atmospheric and tidal changes have certain impacts on the laser ranging accuracy, which indirectly affects laser footprint positioning accuracy. Therefore, auxiliary data processing must be performed before the laser altimeter performs high-precision ground positioning.

a) Precise attitude determination: The GF-7 satellite is equipped with two groups of dual fields of view star-trackers and nine gyroscopes. Star-trackers output the absolute attitude quaternion in the inertial coordinate system at a frequency of 8 Hz. Gyroscopes output the satellite relative attitude angular velocity at a frequency of 16 Hz. The GF-7 satellite downlinks the original attitude measurement data of the whole trace for PAD. The combined attitude determination with the star tracker and gyro data often uses filtering technology to produce the optimal result, which are better results than using a single attitude sensor. Therefore, the filter design and filtering method selection play important roles in the attitude output accuracy [28].

The unscented Kalman filter (UKF) filtering strategy is used for GF-7 satellite attitude processing. This strategy uses the two-direction iterative approximation. Each filtering process includes a forward UKF, a backward UKF, and a covariance weighted smoothing. The smoothed estimates were obtained by averaging the forward and backward state estimates with weights based on their covariances. This approach minimizes the covariances of the averaged estimates. The two filtering processes are independent, and smoothing is performed based on the last two filtering results. Based on this strategy, the three-axis accuracy of the GF-7 satellite attitude can be better than 0.5 arc s. The principle of the UKF filtering strategy is shown in Fig. 7.

In Fig. 7, the suffixes f and b represent forward filtering and backward filtering, respectively. The initial estimated attitude value $\hat{q}_f(0)$ is obtained by dual vector determination with the star tracker observation at the first measurement epoch t_0. The initial estimated value of the gyro bias $\hat{b}_f(0)$ is b_0, which can be analyzed using the downlinked telemetry data. The initial values of the error covariance $\hat{P}_f(0)$ are also obtained from the empirical value of P_0, which is derived from the star tracker/gyro measurements. In addition, the initial estimated value of $\hat{q_b}(N)$ is the star tracker observations $q_N{}^-$ at the last measurement epoch t_N, and the initial estimated values of the gyro bias $\hat{b_b}(N)$ and error covariance $\hat{P}_b(N)$ are obtained from the forward filtering results.

b) Precise orbit determination: The GF-7 satellite is equipped with a dual-frequency GPS receiver, which downlinks original GPS orbit data for the whole track at a frequency of 1 Hz. In addition to providing observation time and spatial data, the orbit perturbation in the GPS observation data directly reflects Earth's gravity field information, which provides higher precision for satellite orbit determination. According to the satellite dynamics principle and the batch processing mode, the SRT will make full use of satellite GPS data for the GF-7 satellite POD based on the simplified dynamics and least square batch processing algorithm [29], [30]. After data processing, the positioning accuracy of the orbit triaxial is better than 10 cm. The POD process of the GF-7 satellite is shown in Fig. 8.

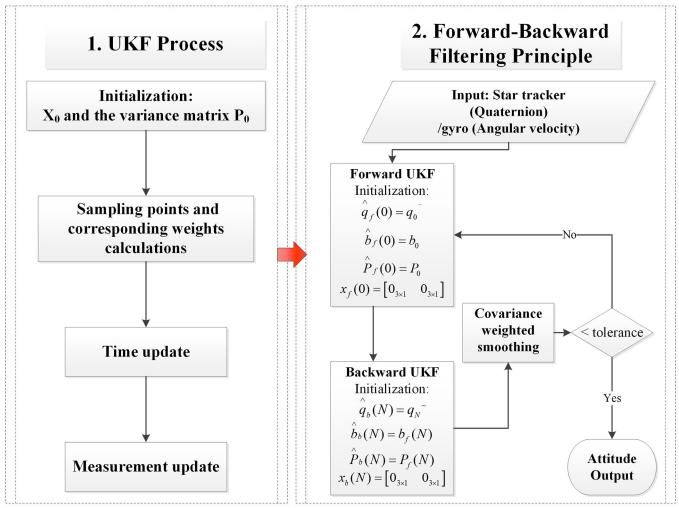

Fig. 7. Principle of the forward–backward UKF.

c) Atmospheric correction: The effects of laser energy attenuation, pulse expansion, optical path refraction, and dispersion are caused by atmospheric molecules, including aerosol, dust, fog, clouds, and other particles. These effects are one of the main error sources of laser ranging accuracy. According to the basic parameters of the GF-7 spaceborne laser altimeter, the zenith delay and off-nadir pointing correction model is used to correct the GF-7 laser atmosphere delay [31].

During the operation of the GF-7 satellite, the weather stations and sounding balloons will be used to obtain atmospheric parameters within the territory of China. The atmospheric parameters at each laser point will be interpolated using National Centers for Environmental Prediction (NCEP) data outside of China.

d) Tidal correction: The tide is mainly divided into sea tide, earth tide, pole tide, and load tide, which causes laser ranging errors by causing the geoidal surface to shift. The earth tide is a regular deformation phenomenon of the surface caused by the periodic tidal forces of the sun, the moon, and other planets on solid earth, with an error up to $\pm$30 cm. The impacts on the laser range are $\pm$50 cm in the wide sea area, $\pm$2 m along the coastline, and $\pm$1 m over the glaciers. The pole tide and load tide contract the earth land surfaces, causing a laser altimetry error less than $\pm$2 cm, which is negligible [32]. The GF-7 laser altimeter mainly considers the correction of the earth tide and sea tide. The SRT will use the earth tide correction model to correct the earth tide. The latest tide model (FES2018) will be used to correct ocean tides in the global region.

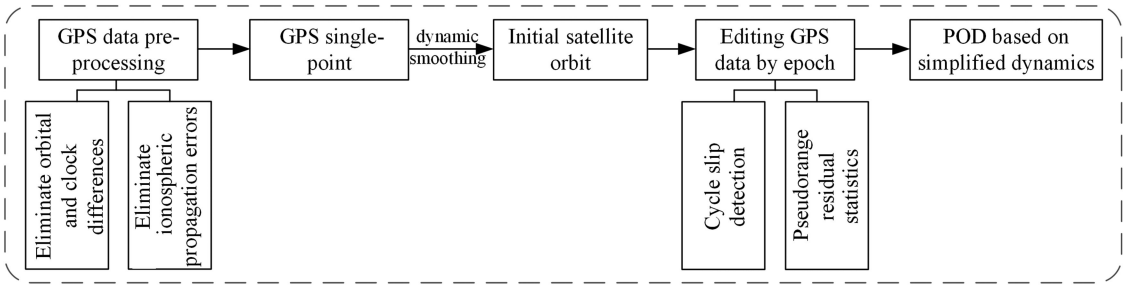

Fig. 8. GF-7 satellite POD process.

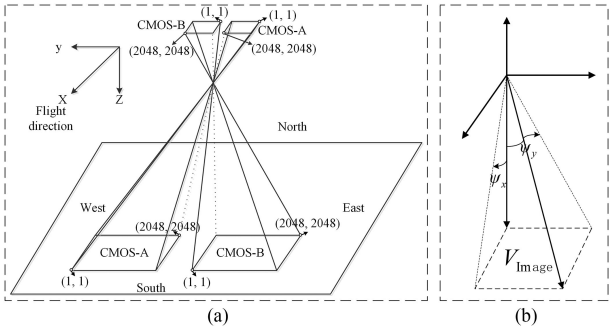

Fig. 9. Schematic diagram of the LFC positioning. (a) LFC geometry installation diagram. (b) Area-array camera with two-dimensional pointing.

C. Geometric Processing of the LFC

The object coordinate of laser point is positioned based on the geometric relationship between the star tracker, the GPS receiver, satellite platform, and LFC. The geolocation diagram of the LFC is shown in Fig. 9.

1) Imaging Model of the LFC: To avoid the instability of the solution caused by excessive parameterization of the strict geometric model, the 2-D look angle model is used as the intrinsic parameters calibration model of the LFC, which is shown in Fig. 9(b). The V_{Image} is the look angle, and ψ_x and ψ_y are look angles of detectors in complementary metal oxide semiconductor (CMOS) camera. Therefore, the geometric calibration of the LFC can recover the pointing vector of each detector in the camera coordinate system when the tangent value of the look angle is determined by extrinsic parameters calibration.

Due to the narrow field of view (FOV) and small various internal errors, the cubic polynomial model with high orthogonality and low correlation is used as the intrinsic parameter's calibration model, and the imaging model of the LFC can be expressed as

$$\begin{bmatrix} \tan[\psi_x(s,l)] \\ \tan[\psi_y(s,l)] \\ -1 \end{bmatrix} = \lambda' R^{\text{cam}}_{\text{body}}(\text{pitch}, \text{roll}, \text{yaw}) \cdot R^{\text{body}}_{J2000} \times \left[R^{J2000}_{\text{WGS}-84} \begin{bmatrix} X_g \\ Y_g \\ Z_g \end{bmatrix} - \begin{bmatrix} X_{\text{body}} \\ Y_{\text{body}} \\ Z_{\text{body}} \end{bmatrix} \right] \quad (3)$$

where (s, l) is the detector coordinate in the image plane coordinate system; $(\text{pitch}, \text{roll}, \text{yaw})$ is the installment angle of the LFC; λ' is the scale factor; $R^{\text{cam}}_{\text{body}}$ is the rotation matrix of the LFC; R^{body}_{J2000} is the measurement matrix of the attitude control system, which represents the rotation relationship from the J2000 coordinate system to the body coordinate system, the J2000 coordinate system is one of the ICRFs; $R^{J2000}_{\text{WGS}-84}$ represents the rotation matrix from the WGS 84 coordinate system to the J2000 coordinate system; $[\, X_{\text{body}}\ Y_{\text{body}}\ Z_{\text{body}}\,]^T$ represents the coordinates of the projection center in the J2000 coordinate system; and $[\, X_g\ Y_g\ Z_g\,]^T$ represents the object square point coordinates in the WGS 84 coordinate system.

2) Estimation of the Geometric Calibration Parameters: In (3), the extrinsic parameter of LFC is $X_E = (\text{pitch}, \text{roll}, \text{yaw})$; and $\tan[\psi_x(s,l)]$ and $\tan[\psi_y(s,l)]$ are shown in the following formula:

$$\left.\begin{aligned} \tan[\psi_x(s,l)] &= a_0 + a_1 \cdot s + a_2 \cdot l + a_3 \cdot s \cdot l + a_4 \cdot s^2 + a_5 \cdot l^2 \\ &\quad + a_6 \cdot s^2 \cdot l + a_7 \cdot s \cdot l^2 + a_8 \cdot s^3 + a_9 \cdot l^3 \\ \tan[\psi_y(s,l)] &= b_0 + b_1 \cdot s + b_2 \cdot l + b_3 \cdot s \cdot l + b_4 \cdot s^2 + b_5 \cdot l^2 \\ &\quad + b_6 \cdot s^2 \cdot l + b_7 \cdot s \cdot l^2 + b_8 \cdot s^3 + b_9 \cdot l^3 \end{aligned}\right\}. \quad (4)$$

We set X_I as intrinsic parameter of LFC, where $X_I = (a_0, a_1, \ldots, a_9, b_0, b_1, \ldots, b_9)$. Then, the error equations are established for intrinsic and extrinsic parameters of LFC as

$$V_i = A_i X - L_i \quad (5)$$

where X is intrinsic and extrinsic parameter correction of LFC and X plus its initial value X^0 is the optimal value of intrinsic or extrinsic parameters; A_i is coefficient matrix of X; and L_i is error vector.

a) Extrinsic parameters calibration: Assume that the initial value of the LFC intrinsic parameters is the true value, when determining the extrinsic parameters of LFC. The X of (5) is the correction of X_E, and X^0 is X^0_E. According to the principle of indirect block adjustment, the least square criterion is used to calculate the three extrinsic parameters iteratively.

b) Intrinsic parameters calibration: Similarly, extrinsic parameters of the LFC are considered as the true value when the intrinsic parameters of LFC are determined. The correction of X_I is taken into (5) as X, and X^0 is X^0_I. In the same way, the

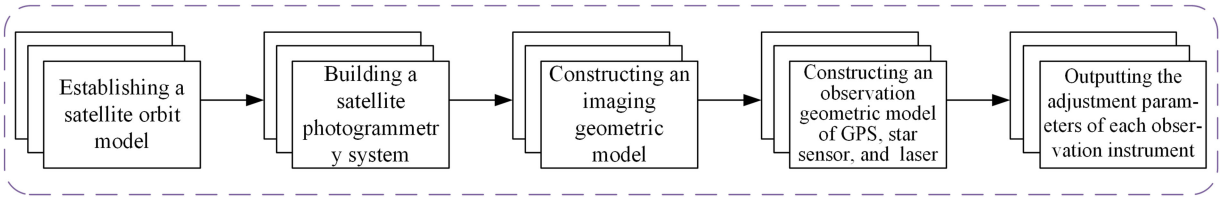

Fig. 10. Technological flow of the combined laser and optical adjustments.

least-square criterion is used to calculate the intrinsic parameters of the LFC iteratively.

3) Image Correction of the Intrinsic Parameters: To express the look angle of each CMOS detector, a binary cubic polynomial is typically used in the generalized body coordinate system of the footprint area array camera. The 2-D look angle model of the intrinsic parameters calibration is shown as follows:

$$\begin{cases} x = (a_0 + a_1 \cdot s + a_2 \cdot l + a_3 \cdot s \cdot l + a_4 \cdot s^2 + a_5 \cdot l^2 \\ \quad + a_6 \cdot s^2 \cdot l + a_7 \cdot s \cdot l^2 + a_8 \cdot s^3 + a_9 \cdot l^3) \cdot f \\ y = (b_0 + b_1 \cdot s + b_2 \cdot l + b_3 \cdot s \cdot l + b_4 \cdot s^2 + b_5 \cdot l^2 \\ \quad + b_6 \cdot s^2 \cdot l + b_7 \cdot s \cdot l^2 + b_8 \cdot s^3 + b_9 \cdot l^3) \cdot f \end{cases} \tag{6}$$

where x, y, and f are interior elements; s and l are sample and line, respectively, in the image plane coordinate system; and a_0–a_9 and b_0–b_9 are the unknown coefficient parameters of the LFC.

The 2-D look angle model can describe the geometric distortion, which is expressed by a strict physical model in the form of an orthogonal polynomial, so that the actual distortion inside the LFC camera can be almost completely recovered by calibration. Due to the characteristics of the LFC, such as the high orbit, narrow FOV, and short focal length, there is a strong correlation among all distortion parameters. However, the significance of some distortion parameters is weak, which makes the estimated results unstable. The essence of the 2-D look angle model normalizes the distortion parameters of the strict physical model by using a set of orthonormal bases to overcome the problem of parameter correlation with the physical model.

D. Combined Laser and Camera Processing

The SRT proposed a laser and optical combined adjustment method based on distance constraints. The basic idea is as follows: a generalized satellite photogrammetric system is constructed that combines the satellite optical camera with other observed payloads similar to the laser. Then, the geometric relationship of each instrument body in the coordinate system measurement, including the optical camera and the laser altimeter, is represented by a strict mathematical geometric model according to the system's geometric installation relationship. The observation equations and their error equations among the satellite cameras, lasers, attitudes, and orbits are derived. These equations can be accurately solved by establishing a combined adjustment model containing original observations of multiple satellite payloads. The adjustment test was carried out under different observation conditions, and then the positioning accuracy of the GF-7 satellite after the adjustment was analyzed. The technical roadmap is shown in Fig. 10.

According to the above basic ideas, combined with the attitude and orbit data, a combined observation equation for the laser and optics is constructed as

$$\begin{cases} V_X = A_{X1}t_1 + A_{X2}t_2 + Ii + Jj + Bb + Cc - L_X \\ V_G = A_{G1}t_1 + A_{G2}t_2 + Dd - L_G \\ V_S = A_S t_2 + Mm - L_S \\ V_L = A_{L1}t_1 + A_{L2}t_2 + Nn + Xx - L_L \end{cases} \tag{7}$$

where V_X is the residual vector of the image point coordinate observation; V_G is the residual vector of the satellite positioning observation; V_S is the residual vector of the satellite attitude observation; V_L is the residual vector of the laser ranging; $A_{X1}, A_{X2}, I, J, B, C, A_{G1}, A_{G2}, D, A_S, M$, and A_{L1}, A_{L2}, N, X represent the coefficient matrix for variables $t_1, t_2, i, j, b, c, d, m, n$ and x; t_1 is the camera orientation line element; t_2 is the camera azimuth element; i is the camera centroid position offset; j is the relative rotation angle of the camera center; b is the image point ground coordinates; c is the camera orientation element; d is the spatial offset of the satellite positioning observation center; m is the attitude rotation angle relative to the camera; n is the offset of the laser fire point; x represents the laser footprint coordinates; and L_X, L_G, L_S, and L_L are the residuals of the observations.

Equation (7) can be converted to matrix form, and its matrix expression is shown as

$$\vec{V} = \vec{A}\vec{X} - \vec{L} \tag{8}$$

where $\vec{V} = [V_X, V_G, V_S V_L]^T$, $\vec{X} = [t_1, t_2, i, j, b, c, d, m, n, x]^T$, $\vec{L} = [L_X, L_G, L_S, L_L]^T$, and

$$\vec{A} = \begin{bmatrix} A_{X1} & A_{X2} & I & J & B & C & 0 & 0 & 0 & 0 \\ A_{G1} & A_{G2} & 0 & 0 & 0 & 0 & D & 0 & 0 & 0 \\ A_S & 0 & 0 & 0 & 0 & 0 & 0 & M & 0 & 0 \\ A_{L1} & A_{L2} & 0 & 0 & 0 & 0 & 0 & 0 & N & X \end{bmatrix}.$$

We can solve the optimal value of $\vec{X}$ in terms of the principle of least squares. The least square solution of the parameter correction is shown in (9). The optimal value is the sum of the initial parameter value and correction value given as

$$\hat{\vec{X}} = (\vec{A}^T P \vec{A})^{-1} (\vec{A}^T P \vec{L}). \tag{9}$$

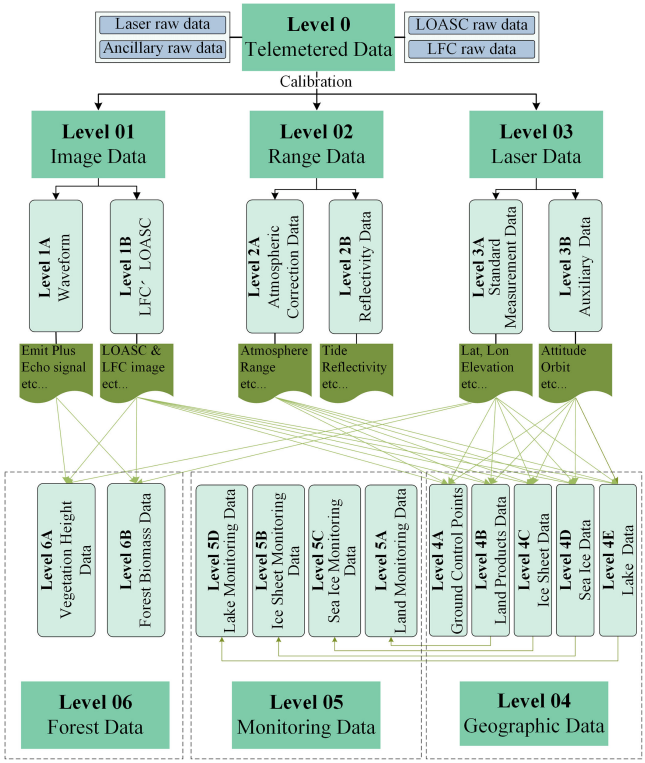

Fig. 11. GF-7 laser altimeter system data product structure.

E. Data Products

The family of the GF-7 laser data products and the connections between them are shown in Fig. 11. The raw data collected by the GF-7 satellite and transmitted to the ground are categorized as the Level 0 product, and these data are archived at the LASAC. The Level 1–3 products are generated directly from the Level 0 product. Level 1–3 products are mainly the basic measurement data of the GF-7 spaceborne laser altimeter system, which includes basic parameters, such as laser point location, waveform, footprint image, attitude, and orbit. Level 4–6 products are thematic data that are derived from the Level 1–3 level products. Only after calibration, GF-7 laser pointing will be precisely determined, and the accurate coordinates of GF-7 laser footprint are easy to know. Then, level 1–6 products are generated based on the GF-7 telemetry data (level 0) after geometric calibration of the laser altimeter.

The GF-7 spaceborne laser altimeter system data are archived by the LASAC. In addition to the Level 0 data product, the Level 1–6 products are expected to be released in the autumn of 2020. Also, we will provide the data to the users worldwide free of charge, after the in-orbit test period. These data will serve users worldwide, and users can log into the LASAC cloud website to download the required data[1] and we will provide a description of the download method on the official website when the laser data are released. However, the detailed product format corresponding to these data, the GF-7 satellite progress status, and related scientific research will be published on the LASAC's official website.[2].

[1]Online. [Available]: http://sasclouds.com/english/home
[2]Online. [Available]: http://www.lasac.cn/

IV. Conclusion

This article provides a detailed introduction to China's first spaceborne laser altimeter system officially for Earth observations, and it includes laser altimeter, LFC, and LOASC. The SRT conducted rigorous test and analysis of the various parameters, and verified the performance indicators of the GF-7 spaceborne laser altimeter system. For the new laser altimeter system, this article introduces three kinds of geometric processing methods: laser geometry processing, LFC geometric processing, and combined laser and camera mapping processing. At the same time, other data processing methods, such as waveform processing, as well as GF-7 satellite precise orbit, precise attitude, atmosphere, and tidal auxiliary parameter correction methods are also introduced. The GF-7 spaceborne laser altimeter system data products are divided into Levels 1–6, which will be released for global use in 2020. The laser altimeter system will play a vital role in global climate change monitoring, surface observation, and environmental protection, especially for the monitoring of glacial reserves in the Antarctic and Arctic.

References

[1] X. Gu and X. Tong, "Overview of China earth observation satellite programs [space agencies]," *IEEE Geosci. Remote Sens. Mag.*, vol. 3, no. 3, pp. 113–129, Sep. 2015.
[2] C. Liu, X. Huang, Z. Zhu, H. Chen, X. Tang, and J. Gong, "Automatic extraction of built-up area from ZY3 multi-view satellite imagery: Analysis of 45 global cities," *Remote Sens. Environ.*, vol. 226, pp. 51–73, Apr. 2019, doi: 10.1016/j.rse.2019.03.033.
[3] X. Huang, D. Wen, J. Li, and R. Qin, "Multi-level monitoring of subtle urban changes for the megacities of China using high-resolution multi-view satellite imagery," *Remote Sens. Environ.*, vol. 196, pp. 56–75, Jul. 2017, doi: 10.1016/j.rse.2017.05.001.
[4] X. Huang, H. Chen, and J. Gong, "Angular difference feature extraction for urban scene classification using ZY-3 multi-angle high-resolution satellite imagery," *ISPRS J. Photogramm. Remote Sens.*, vol. 135, pp. 127–141, Jan. 2018, doi: 10.1016/j.isprsjprs.2017.11.017.
[5] C. A. Shuman *et al.*, "ICESat Antarctic elevation data: Preliminary precision and accuracy assessment," *Geophys. Res. Lett.*, vol. 33, no. 7, Jun. 2006, Art. no. L07501, doi: 10.1029/2005gl025227.
[6] M. A. Lefsky *et al.*, "Estimates of forest canopy height and aboveground biomass using ICESat," *Geophys. Res. Lett.*, vol. 32, no. 22, May 2005, Art. no. L22S02, doi: 10.1029/2005gl023971.
[7] R. S. Lancaster, J. D. Spinhirne, and S. P. Palm, "Laser pulse reflectance of the ocean surface from the GLAS satellite lidar," *Geophys. Res. Lett.*, vol. 32, no. 22, May 2005, Art. no. L22S10, doi: 10.1029/2005GL023732.
[8] H. Zhou, Y. Chen, J. Hyyppä, and S. Li, "An overview of the laser ranging method of space laser altimeter," *Infrared Phys. Technol.*, vol. 86, pp. 147–158, Nov. 2017, doi: 10.1016/j.infrared.2017.09.011.
[9] J. Xie *et al.*, "In-orbit geometric calibration and experimental verification of the ZY3-02 laser altimeter," *Photogrammetric Rec.*, vol. 33, no. 163, pp. 341–362, Sep. 2018, doi: 10.1111/phor.12249.
[10] X. Tang, J. Xie, X. Gao, F. Mo, W. Feng, and R. Liu, "The in-orbit calibration method based on terrain matching with pyramid-search for the spaceborne laser altimeter," *IEEE J. Sel. Topics Appl. Earth Observ. Remote Sens.*, vol. 12, no. 3, pp. 1053–1062, Mar. 2019.
[11] J. Xie *et al.*, "ZY3-02 laser altimeter footprint geolocation prediction," *Sensors*, vol. 17, no. 10, p. 2165, Sep. 2017, doi:10.3390/s17102165.
[12] G. Zhang *et al.*, "Geometric calibration and validation of ZY3-02 satellite laser altimeter system," *Geomatics Inf. Sci. Wuhan Univ.*, vol. 42, no. 11, pp. 1589–1596, Jun. 2017, doi: 10.11947/j.AGCS.2017.20160597.
[13] L. Song, Y. Hong, M. Yue, H. Ke, Z. Hui, and S. Guang-Yuan, "On-orbit calibration of satellite laser altimeters based on footprint detection," *Acta Physica Sinica*, vol. 66, no. 13, 2017, Art. no. 134206.
[14] L. A. Magruder, C. E. Webb, T. J. Urban, E. C. Silverberg, and B. E. Schutz, "ICESat altimetry data product verification at white sands space harbor," *IEEE Trans. Geosci. Remote Sens.*, vol. 45, no. 1, pp. 147–155, Jan. 2007.

[15] Y. Ma*et al.*, "Method for determining the footprint center of a satellite laser altimeter based on marked waveforms by CCRs," *Appl. Opt.*, vol. 57, no. 30, pp. 8928–8935, Oct. 2018, doi: 10.1364/AO.57.008928.
[16] R. Liu *et al.*, "Waveform simulation of spaceborne laser altimeter echo based on fine terrain," *Acta Photonica Sinica*, vol. 47, no. 11, pp. 79–88, Nov. 2018, doi: 10.3788/gzxb20184711.1128004.
[17] J. B. Blair and M. A. Hofton, "Modeling laser altimeter return waveforms over complex vegetation using high-resolution elevation data," *Geophys. Res. Lett.*, vol. 26, no. 16, pp. 2509–2512, 1999.
[18] C. F. Martin *et al.*, "ICESat range and mounting bias estimation over precisely-surveyed terrain," *Geophys. Res. Lett.*, vol. 32, p. L21S07, May 2005, doi: 10.1029/2005GL023800.
[19] S. Q. Tian, *Geometric Calibration and Validation of Domestic Space-Borne Laser Altimeter*. Shaanxi, China: Chang'an University, 2017.
[20] D. V. Hieu, *Processing and Application of ICESat Large Footprint Full Waveform Laser Range Data*. Delft, The Netherlands: Delft University of Technology, 2010.
[21] G. Sun *et al.*, "Forest vertical structure from GLAS: An evaluation using LVIS and SRTM data," *Remote Sens. Environ.*, vol. 112, no. 1, pp. 107–117, Jan. 2008, doi: 10.1016/ j.rse.2006.09.036.
[22] M. Hollaus *et al.*, "Accuracy of large-scale canopy heights derived from LiDAR data under operational constraints in a complex alpine environment," *ISPRS J. Photogramm. Remote Sens.*, vol. 60, no. 5, pp. 323–338, Aug. 2006, doi: 10.1016/j.isprsjprs.2006.05.002.
[23] T. Zhou *et al.*, "Gold – A novel deconvolution algorithm with optimization for waveform LiDAR processing," *ISPRS J. Photogramm. Remote Sens.*, vol. 129, pp. 131–150, Jul. 2017, doi: 10.1016/j.isprsjprs.2017.04.021.
[24] C. Wang, F. Tang, L. Li, G. Li, F. Cheng, and X. Xi, "Wavelet analysis for ICESat/GLAS waveform decomposition and its application in average tree height estimation," *IEEE Geosci. Remote Sens. Lett.*, vol. 10, no. 1, pp. 115–119, Jan. 2013.
[25] M. A. Hofton, J. B. Minster, and J. B. Blair, "Gaussian decomposition of laser altimeter waveforms," *IEEE Trans. Geosci. Remote Sens.*, vol. 38, no. 4, pp. 1989–1996, Aug. 1999.
[26] L. Hua, "Quantification of analytes in overlapping peaks from capillary electrophoresis using multivariate curve resolution-alternating least squares methods," *Electrophoresis*, vol. 18, no. 24, pp. 3107–3115, 2003, doi: 10.1002/elps.200305426.
[27] Y. Wang *et al.*, "Slope-adaptive waveform metrics of large footprint lidar for estimation of forest aboveground biomass," *Remote Sens. Environ.*, vol. 224, pp. 386–400, Apr. 2019, doi: 10.1016/j.rse.2019.02.017.
[28] X. Tang *et al.*, "High-precision attitude post-processing and initial verification for the ZY-3 satellite," *Remote Sens.*, vol. 7, no. 1, pp. 111–134, Dec. 2014, doi: 10.3390/rs70100111.
[29] C. M. Zhao and X. M. Tang, "Precise orbit determination for the ZY-3 satellite mission using GPS receiver," *J. Astronaut*, vol. 34, no. 9, pp. 1202–1206, Sep. 2013, doi: 10.3873/j.issn.1000-1328.2013.09.004.
[30] Q. L. Zhao *et al.*, "Determination of precise orbit using onboard GPS data for gravity modeling oriented satellites," *Geomatics Inf. Sci. Wuhan Univ.*, vol. 33, no. 8, pp. 810–814, Aug. 2008.
[31] T. A. Herring and K. J. Quinn, "The algorithm theoretical basis document for the atmospheric delay correction to GLAS laser altimeter ranges," NASA Goddard Space Flight Center, 2012. [Online]. Available: https://ntrs.nasa.gov/search.jsp?R=20130001652
[32] H. A. Fricker *et al.*, "The algorithm theoretical basis document for tidal corrections," NASA Goddard Space Flight Center, 2012. [Online]. Available: https://ntrs.nasa.gov/search.jsp?R=20130013632

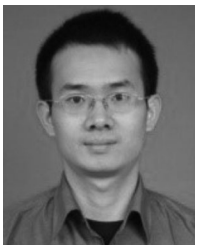

Junfeng Xie received the B.S. and Ph.D. degrees in remote sensing information engineering from the Wuhan University, Wuhan, China, in 2004 and 2009, respectively.

He is currently a Senior Researcher with the Land Satellite Remote Sensing Application Center (LASAC), Ministry of Natural Resources of P.R. China. His research interests include satellite attitude determination, spaceborne laser altimeter calibration, and remote sensing application.

Dr. Xie is the Academic Leader of the LASAC, the Young Academic Leader of the NASG, and the Deputy Director of Calibration Department, LASAC.

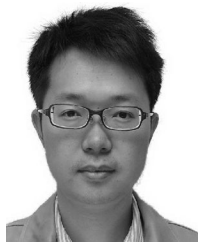

Genghua Huang received the Ph.D. degree in physical electronics from the Chinese Academy of Sciences, Beijing, China, in 2007.

He is currently a Senior Researcher with the Shanghai Institute of Technical Physics, Chinese Academy of Science, and the Deputy Director of the designers of the GF-7 laser altimeter system. His research interests include spaceborne laser payloads, photon counting lidar system, and active remote sensing.

Ren Liu received the M.S. degree from the School of Geomatics, Liaoning Technical University, Liaoning, China, in 2019. He is currently working toward the Ph.D. degree with the School of Earth Sciences and Engineering, Hohai University, Nanjing, China.

His research interests include laser waveform processing and geometric calibration of spaceborne laser altimeter.

Chenguang Zhao, photograph and biography not available at the time of publication.

Jun Dai, photograph and biography not available at the time of publication.

Taoyong Jin, photograph and biography not available at the time of publication.

Fan Mo, photograph and biography not available at the time of publication.

Ying Zhen, photograph and biography not available at the time of publication.

Shaoli Xi, photograph and biography not available at the time of publication.

Hongzhao Tang, photograph and biography not available at the time of publication.

Xianhui Dou, photograph and biography not available at the time of publication.

Chenchen Yang, photograph and biography not available at the time of publication.